J Mol Model (2013) 19:3805–3812
DOI 10.1007/s00894-013-1901-1

ORIGINAL PAPER

# Electronic structure and optical properties of Cu-doping and Zn vacancy impurities in ZnTe

**Qing-Fang Li · Ge Hu · Qing She · Jing Yao · Wen-Jiang Feng**

Received: 31 March 2013 / Accepted: 27 May 2013 / Published online: 25 June 2013


**Abstract** The geometric structures of perfect ZnTe, that with Zn vacancy ($Zn_{0.875}Te$), and Cu-doped ZnTe ($Zn_{0.875}Cu_{0.125}Te$) were optimized using the pseudopotential plane wave (PP-PW) method based on the density functional theory (DFT) within generalized gradient approximation (GGA). The cohesive energy, band structure, density of states, and Mulliken populations were calculated and discussed in detail. On the other hand, an accurate calculation of linear optical functions (the dielectric function, refraction index, reflectivity, conductivity function, and energy-loss spectrum) was performed. The results demonstrated that compared to the perfect ZnTe, the lattice parameters of $Zn_{0.875}Te$ and $Zn_{0.875}Cu_{0.125}Te$ were changed and the cell volumes decreased to some extent due to the vacancy and introduction of impurity. A vacancy acceptor level and an acceptor impurity level were produced in $Zn_{0.875}Te$ and $Zn_{0.875}Cu_{0.125}Te$, respectively. By comparison, Cu doping in the ZnTe system is relatively stable while the monovacancy system is not.

**Keywords** Electronic structure · First-principles · Impurities · Optical properties · ZnTe

## Introduction

Zinc telluride (ZnTe), an II–VI semiconductor material with a band-gap of 2.26 eV at room temperature, can be well codoped with transition metals such as Co, Mn, Fe and Ni [1–3]. Recently, researchers from domestic and overseas have attached importance to ZnTe as it has high potential and attraction for optoelectronic applications such as light sensitive ceramics, piezoelectric devices and solar cells *etc*. [4, 5]. In the recent ten years, considerable theoretical and experimental efforts have been devoted to determine the electronic and optical properties of ZnTe system materials in order to design novel semiconductor materials. Recently, Joshi KB et al. [6] have studied the electronic band structures and electron momentum density distrubution of ZnTe, and they also presented the band-by-band decomposition of autocorrelaion functions as well as directional Compton profiles. The electronic structure and magnetic properties of ZnTe thin film doped with 3d transition metals (TM = Cr and Mn) have been studied by Zhou and the coworkers [7] with *ab initio* calculations, whose careful analysis of the electronic structure revealed that the hybridization between Cr *3d* (Mn *3d*) and Te *5p* was found to be responsible for the ferromagnetic (FM). Identically by *ab initio* calculations, Szwacki et al. [8] investigated the structural properties of ZnTe, MnTe, and $Mn_{1-x}Zn_xTe$ alloy with zinc-blende, NiAs, and wurtzite phases, and predicted that the zinc-blende phase is more stable than wurtzite for all compositions. Uspenskiia et al. [9] calculated the electronic structure and magnetic properties of $Ga_{1-x}Mn_xAs$, $Ga_{1-x}Mn_xN$, $Zn_{1-x}M_xO$, and $Zn_{1-x}M_xTe$ (M=V,Cr, Mn, Fe, and Co) diluted magnetic semiconductors (DMS) in the 64 atom supercell with another calculation method known as the tight-binding LMTO method, the results showed that the stability of the ferro- and antiferromagnetic (FM and AFM) states in DMS strongly correlates with the occupation and energy position of *3d*-dopant bands. Tablero et al. [10] presented the total energy calculations to analyze the electronic properties of the O-doped ZnTe ($ZnTe_{1-x}O_x$) alloys. Besides, Boyer-Richard et al. [11] have performed accurate tight binding simulations to design type-II short-period CdSe/ZnTe superlattices suited for photovoltaic applications.

Q.-F. Li · G. Hu (✉) · Q. She · J. Yao
School of Chemistry and Chemical Engineering, Chongqing University, Chongqing 400044, People's Republic of China
e-mail: cqdxhuge@163.com

W.-J. Feng
College of Physics Science and Technology, Shenyang Normal University, Shenyang 110034, People's Republic of China

According to the efforts of the researchers, the dopants remarkably affect the electronic and optical properties of ZnTe system materials. Although experimenters have tried their best to realize the high quality ZnTe conductivity via introducing probable dopants, very few workers have researched the microcosmic structures and properties of the optimized ZnTe with impurity Cu, and the origin of the doping difficulties yet remains unclear. Recently, we performed density functional calculations on the zinc vacancy and Cu-doping ZnTe in order to contribute to a better understanding of defect mechanism. In the present article, based on the first-principles within the DFT, we calculated and analyzed the electronic properties such as band structure, density of states and Mulliken populations of the perfect zinc blend ZnTe, that with Zn vacancies ($Zn_{0.875}Te$) and Cu impurity ($Zn_{0.875}Cu_{0.125}Te$). According to the precisely calculated results, we also investigated the optical properties including dielectric function, loss function, optical conductivity, refractive index and reflectivity of the three systems. Comparisons have been made wherever possible with the experimental and previously reported theoretical data.

## Computational details

Ideal ZnTe in cubic zinc-blende (ZB) structure belongs to $F\overline{4}3m$ (No.216) space group, $T_d^2$ symmetry system, and the values of cell parameters $a$, $b$, $c$, $\alpha$, $\beta$, and $\gamma$ are as follows: $a = b = c = 6.101$ Å, $\alpha = \beta = \gamma = 90°$ [12]. All configurations were simulated within a ZnTe supercell, which is equivalent to a $2\times1\times1$ primitive cell and contains 16 atoms with periodic boundary conditions applied. The Zn (0.5, 0.5, 0.5) atom was substituted by Cu atom or removed when doping or creating vacancy. In addition, as displayed in Fig. 1, depending on the atom location, we divided Zn atoms into four categories: ZnI (vertex atom), ZnII (midpoint atom), ZnIII (centroid atom), and ZnIV (the rest Zn atoms), and two groups for Te atoms: TeI (the nearest Te atoms around the vacancy or impurity Cu atom) and TeII (the remaining Te atoms).

All calculations were performed using a pseudopotential plane wave (PP-PW) method as implemented in CASTEP [13] code. We employed the Vanderbilt-type ultrasoft pseudopotentials [14] to treat the interaction between valence electrons and ions. The electronic exchange-correlation function was treated within the GGA of Perdew, Burke and Ernzerhof (GGA-PBE) [15]. Zn $3d^{10}4s^2$, Te $5s^25p^4$, and Cu $3d^{10}4s^1$ were treated as valence states in consideration of their relatively high energies. The cutoff energy was 400 eV and a $2\times4\times4$ Monkhorst-Pack [16] $k$-points grid was adopted for integration in the first Brillouin zone (BZ). The Broyden-Fletcher-Goldfarb-Shanno (BFGS) minimization technique [17], which provides a fast way of finding the lowest energy structure, was used in the geometry optimization. The tolerances for geometry optimization were set as the difference in total energy being within $5.0\times10^{-6}$ eV·atom$^{-1}$, the maximum ionic Hellmann- Feynman force within 0.01 eV·Å$^{-1}$, the maximum ionic displacement within $5.0\times10^{-3}$ Å, and the maximum stress within 0.02 GPa.

The calculation of optical properties usually requires a dense mesh of uniformly distributed $k$-points. Thus, we employ BZ integration with a $20\times20\times20$ grid of Monkhorst-Pack points for the calculation. Optical properties can be determined using the complex dielectric function $\varepsilon(\omega)=\varepsilon_1(\omega)+i\varepsilon_2(\omega)$ [18], which is mainly connected with the electronic structures. The imaginary part of the dielectric function $\varepsilon_2(\omega)$ was calculated from the momentum matrix elements between the occupied and unoccupied wave functions [19] as follows:

$$\varepsilon_2(\omega) = \frac{Ve^2}{2\pi\hbar m^2\omega^2}\int d^3k\sum_{n,n'}\left|\left\langle\vec{k}n\right|\left|\vec{p}\right|\left.\vec{k}n'\right\rangle\right|^2 \times f\left(\vec{k}n\right)\left[1-f\left(\vec{k}n'\right)\right]\delta\times\left(E_{\underset{kn}{\rightarrow}}-E_{\underset{kn'}{\rightarrow}}-\hbar\omega\right), \quad (1)$$

where $e$ is the electron charge, $m$ is the electron mass, $V$ is the unit cell volume, $\omega$ is the photon frequency, $\vec{p}$ is the momentum operator, $\hbar\omega$ is the energy of the incident phonon, $\vec{k}n$ and $\vec{k}n'$ are the conduction band (CB) and valence band (VB) wave functions corresponding to the $n$th and $n'$ th eigenvalue with crystal momentum $k$, and $f(\vec{k}n)$ is the Fermi distribution function. The real part of the dielectric function $\varepsilon_1(\omega)$ can be attracted from $\varepsilon_2(\omega)$ by using the Kramers-Kronig relationship [20]:

$$\varepsilon_1(\omega) = 1 + \frac{2}{\pi}p\int_0^\infty \frac{\varepsilon_2(\omega')\omega' d\omega'}{\omega'^2-\omega^2}, \quad (2)$$

where $p$ is the principal value of the integral. The knowledge of both the imaginary and real parts of the dielectric function allows the calculation of the other optical properties such as the conductivity function $\sigma(\omega)$, reflectivity $R(\omega)$, refractive index $n(\omega)$, and energy-loss spectrum $L(\omega)$ [21, 22].

$$\sigma(\omega) = \frac{\omega}{4\pi}\varepsilon_2(\omega) + i\left(\frac{\omega}{4\pi} - \frac{\omega}{4\pi}\varepsilon_1(\omega)\right) \quad (3)$$

$$R(\omega) = \left|\frac{\sqrt{\varepsilon(\omega)}-1}{\sqrt{\varepsilon(\omega)}+1}\right|^2 \quad (4)$$

$$n(\omega) = \left[\frac{\varepsilon_1(\omega)}{2} + \frac{\sqrt{\varepsilon_1^2(\omega)+\varepsilon_2^2(\omega)}}{2}\right]^{1/2} \quad (5)$$

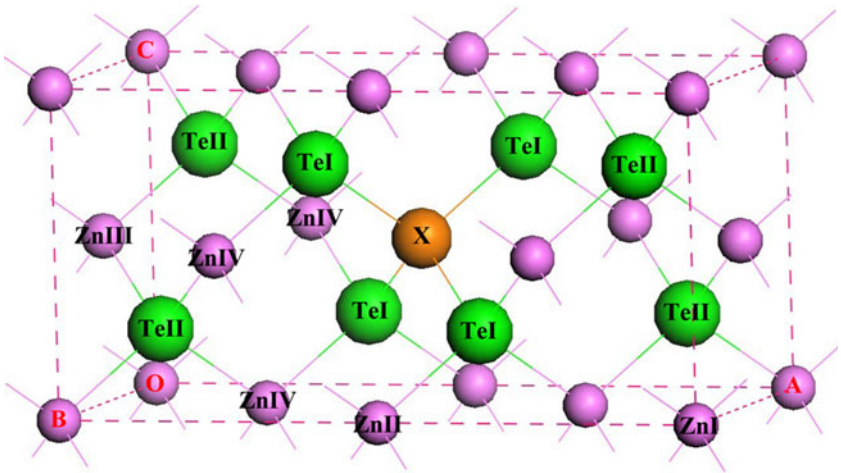


**Fig. 1** 2×1×1 supercell structure of ZnTe with defect (X = vacancy or impurity Cu atom)

$$L(\omega) = \frac{\varepsilon_2(\omega)}{\varepsilon_1^2(\omega) + \varepsilon_2^2(\omega)} \quad (6)$$

## Results and discussion

### Structural properties

Firstly, the three periodic supercells of ZnTe were optimized for testing the validity of the method. Table 1 summarizes the equilibrium lattice constants of pure and defective ZnTe systems. Our calculation for pure ZnTe is slightly beyond the experimental value [12]. This overestimation of the lattice constants based on GGA approximation is reasonable, which is known to result from the discontinuity of the exchange-correlation energy [23]. However, it is in good agreement with other theoretical result [24]. $Zn_{0.875}Te$ has a smaller volume than pure ZnTe, which is derived from the vacancy. As for $Zn_{0.875}Cu_{0.125}Te$, the volume reduction results from the minor difference in atomic radius between Cu and Zn atoms, the local structure around the Cu dopant is slightly suppressed as the Te atoms are drawn closer to the Cu atom after geometry optimization, for which evidence can be also found in Table 3.

The cohesive energy is a measure of the strength of the forces which is calculated by using the Eq. (7):

$$E_{coh} = (E_{tot} - N_a E_a - N_b E_b - N_c E_c)/(N_a + N_b + N_c), \quad (7)$$

where $E_{tot}$ is the total energy of the compound at the equilibrium lattice constant, and $E_a$, $E_b$, and $E_c$ are the energies of the isolated atoms $a$, $b$, and $c$ in the freedom states, respectively. $N_a$, $N_b$, and $N_c$ refer to the numbers of $a$, $b$, and $c$ atoms in each unit cell, respectively [25]. The computed cohesive energies for the three structures are listed in Table 1. Further analysis shows that $Zn_{0.875}Cu_{0.125}Te$ has the most stable structure due to the highest absolute value of cohesive energy and ZnTe has relatively weaker structure stability, while the structure stability of $Zn_{0.875}Te$ is the worst due to the lowest absolute value of cohesive energy. This also indicates that Cu doping in the ZnTe system is relatively stable while the monovacancy system is not.

### Electronic structures

Figure 2(a–c) presents the calculated energy band structures along the high symmetry directions in the first BZ for ZnTe, $Zn_{0.875}Te$, and $Zn_{0.875}Cu_{0.125}Te$, respectively. Basically, the energy structure of compounds depends on the interactions between orbitals in the lattice. It's obvious that the valence band maximum (VBM) and conduction band minimum (CBM) occur at the same $k$-point (G) for all the three cells, indicating that they are all direct band gap semiconductors. The calculated band gaps are 1.054 eV, 1.319 eV, and 0.960 eV for ZnTe, $Zn_{0.875}Te$, and $Zn_{0.875}Cu_{0.125}Te$, respectively. It is clearly seen that the calculated band gap for ZnTe, as expected, is underestimated in comparison with experiment data (2.28 eV) [26], however, it agrees well with other

**Table 1** Optimized geometric lattice parameters of perfect and defective ZnTe systems

| | Present | | | | Expt.[12] | Other cal.[24] | $E_{coh}$ (eV/atom) |
|---|---|---|---|---|---|---|---|
| | $a$/Å | $b$/Å | $c$/Å | $V$/Å$^3$ | $c$/Å | $c$/Å | |
| ZnTe | 12.387 | 6.194 | 6.194 | 475.221 | 6.101 | 6.200 | −2.88 |
| $Zn_{0.875}Te$ | 12.155 | 6.086 | 6.086 | 450.252 | | | −2.86 |
| $Zn_{0.875}Cu_{0.125}Te$ | 12.317 | 6.151 | 6.151 | 465.983 | | | −2.99 |

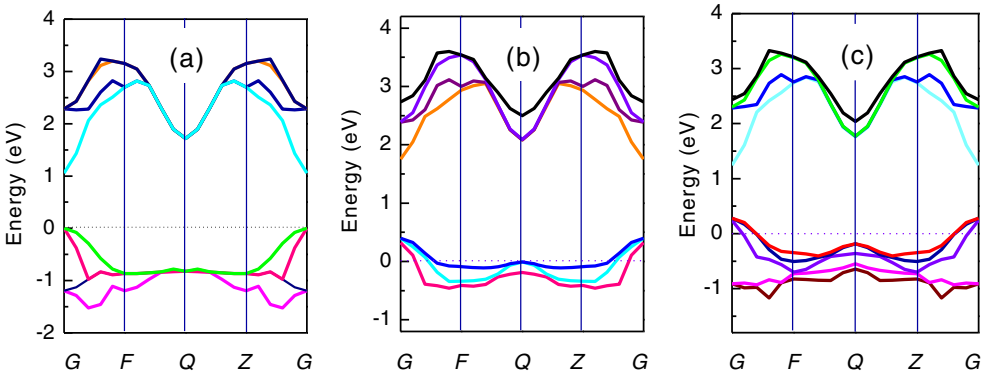


**Fig. 2** Calculated electronic band structures for **a** perfect ZnTe, **b** $Zn_{0.875}Te$, **c** $Zn_{0.875}Cu_{0.125}Te$. The Fermi level is set to zero

theoretical results [22, 24]. This underestimation of the band gaps is mainly due to the fact that the simple form of GGA do not take into account the quasiparticle self-energy correctly which make it not sufficiently flexible to accurately reproduce both exchange correlation energy and its charge derivative [27].

In order to elucidate the major contribution of orbit in the band structure, the total and atom-resolved density of states (DOS) are calculated and plotted in Fig. 3. Likewise, a band gap at the Fermi level can be observed for the three crystals. As shown in Fig. 3(a), the DOSs indicate that ZnTe CBs originate mainly from the cooperative contributions of Zn 3*d*, Te 5*s*, and Te 5*p* orbitals, among which Zn atoms are dominant. VBs between −11.5 eV and −10.0 eV are derived from Te 5*s* orbital. This band is somewhat isolated and far away from the other bands that we will pay little attention to it. The major contributions to VBs between −7.0 eV and −5.8 eV are mainly from the localized Zn 3*d* orbitals. The upper VBs from −5.0 to 0.0 eV are predominantly composed of Se 4*p* states.

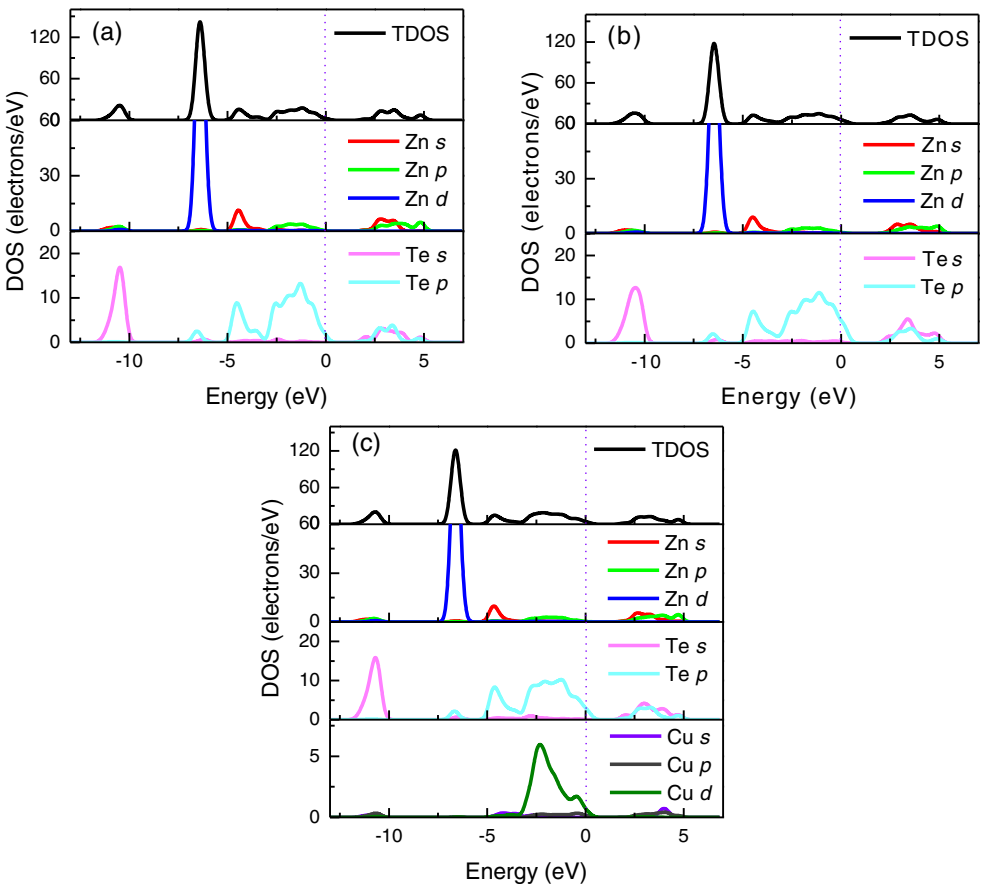


**Fig. 3** Calculated total and partial densities of states for **a** perfect ZnTe, **b** $Zn_{0.875}Te$, and **c** $Zn_{0.875}Cu_{0.125}Te$. The vertical line at zero point energy is aligned at the Fermi level

**Table 2** Mulliken atomic population analysis of Zn, Te, and Cu atoms

| | Ion | Species | *s* | *p* | *d* | Total | Charge |
|---|---|---|---|---|---|---|---|
| ZnTe | Zn | – | 0.94 | 1.25 | 9.98 | 12.17 | −0.17 |
| | Te | – | 1.51 | 4.32 | 0.00 | 5.83 | 0.17 |
| $Zn_{0.875}Te$ | Zn | ZnI | 0.89 | 1.26 | 9.98 | 12.13 | −0.13 |
| | | ZnII | 1.12 | 1.31 | 9.98 | 12.41 | −0.41 |
| | | ZnIII | 0.97 | 1.25 | 9.98 | 12.21 | −0.21 |
| | | ZnIV | 1.00 | 1.28 | 9.98 | 12.26 | −0.26 |
| | Te | TeI | 1.55 | 4.21 | 0.00 | 5.76 | 0.24 |
| | | TeII | 1.52 | 4.27 | 0.00 | 5.79 | 0.21 |
| $Zn_{0.875}Cu_{0.125}Te$ | Cu | – | 0.83 | 1.02 | 9.75 | 11.60 | −0.60 |
| | Zn | ZnI | 0.93 | 1.26 | 9.98 | 12.17 | −0.17 |
| | | ZnII | 0.96 | 1.26 | 9.98 | 12.20 | −0.20 |
| | | ZnIII | 0.94 | 1.24 | 9.98 | 12.16 | −0.16 |
| | | ZnIV | 0.94 | 1.26 | 9.98 | 12.19 | −0.19 |
| | Te | TeI | 1.46 | 4.24 | 0.00 | 5.17 | 0.29 |
| | | TeII | 1.53 | 4.29 | 0.00 | 5.82 | 0.18 |

As presented in Fig. 3(b), compared with those of perfect ZnTe, Te *5s* states of $Zn_{0.875}Te$ shift to upper energy range and the vacancy orbital appears in the vicinity of the Fermi energy, which can be considered to be caused by the lone unpaired valence electrons of Te atoms. And the differences caused by electron deficiency will strongly affect the optical properties. For which theoretical calculations have predicted that the zinc vacancy in $Zn_{0.875}Te$ may form shallow acceptor level and make them *n*-type conductivity. Had the VBM consisted of anion orbitals alone, one would except roughly similar band gaps in ZnTe and $Zn_{0.875}Cu_{0.125}Te$, since the Cu *s*-orbital energies are close to those of Zn. The band structure and DOSs indicates that $Zn_{0.875}Cu_{0.125}Te$ has a narrower band gap (0.960 eV), and the energy of the VBM rises to 0.283 eV, as shown in Figs. 2(c) and 3(c). Then a deep acceptor impurity level was produced in $Zn_{0.875}Cu_{0.125}Te$. The appropriate explanation seems to be the *p-d* repulsion effect [28], which can be described as that the Cu 3*d* orbitals in $Zn_{0.875}Cu_{0.125}Te$ are considerably closer in energy to the Te 5*p* orbitals than that of Zn 3*d* orbitals, thus leading to a far more effective *p-d* repulsion. And hence with a remarkable reduction in the band gap due to the fact that the Cu 3*d* orbitals are also more delocalized than the Zn 3*d* orbitals, which lead to the formation of a larger coupling matrix element in $Zn_{0.875}Cu_{0.125}Te$ and a larger *p-d* repulsion.

In addition, we also calculated Mulliken populations for the materials of interest on the grounds that this helps to understand bonding behavior, as listed in Tables 2 and 3. As listed in Table 2, Mulliken atomic population analysis of all the present atoms has been performed for further study of the structural relaxation. The same atoms can have diverse charge distributions because of their different sites. In $Zn_{0.875}Te$, the Te atoms seemingly can not hold onto their electrons tightly, as indicated by statistics showing increased absolute values of charge for Te atoms, whether close to the vacancy center or not, and it is noteworthy that Te(I) atoms increased slightly more than others due to a lack of Zn atom. For $Zn_{0.875}Cu_{0.125}Te$, the Te(I) charge changes sharply, the charge of Cu is negative(−0.60), indicating that the electronegativity of Cu is greater than Zn, consequently, it is more difficult to lose electrons.

**Table 3** Mulliken bond population analysis of Zn−Te and Cu−Te bonds

| | | ZnI−TeII | ZnIII−TeII | ZnIV−TeII | ZnII−TeI | ZnIV−TeI | Cu−TeI |
|---|---|---|---|---|---|---|---|
| ZnTe | Population | 0.50 | 0.50 | 0.50 | 0.50 | 0.50 | |
| | Length/Å | 2.682 | 2.682 | 2.682 | 2.682 | 2.682 | |
| $Zn_{0.875}Te$ | Population | 0.39 | 0.37 | 0.26 | 0.15 | 0.32 | |
| | Length/Å | 2.664 | 2.681 | 2.678 | 2.657 | 2.645 | |
| $Zn_{0.875}Cu_{0.125}Te$ | Population | 0.47 | 0.38 | 0.43 | 0.14 | 0.30 | 0.57 |
| | Length/Å | 2.673 | 2.687 | 2.678 | 2.687 | 2.669 | 2.577 |

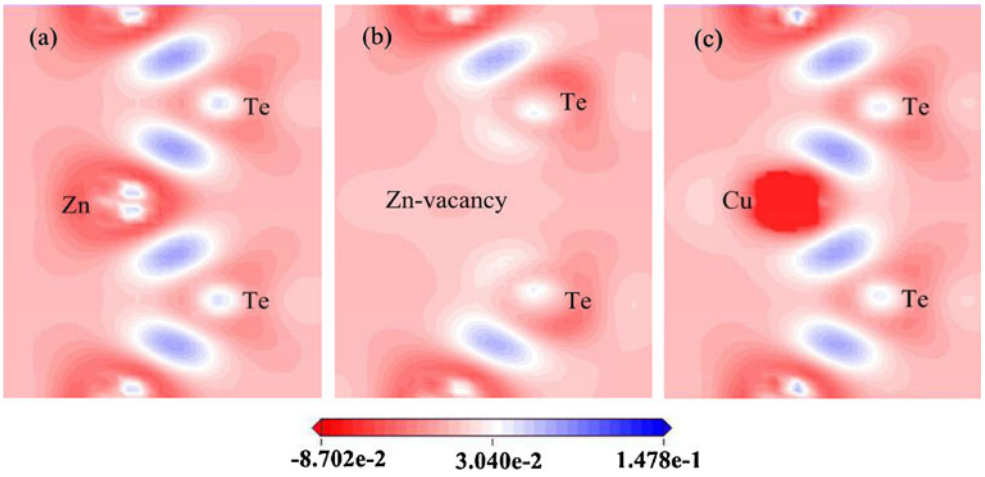


**Fig. 4** Electron density difference map for **a** perfect ZnTe, **b** $Zn_{0.875}Te$, and **c** $Zn_{0.875}Cu_{0.125}Te$ plotted from −0.08702 (*red*) to 0.1478 (*blue*) e·Å$^{-3}$

In addition to providing an objective criterion for bonding between atoms, the overlap population may be used to assess the covalent or ionic nature of a bond. A high value of the bond population indicates a covalent bond, while a low value indicates an ionic interaction. Positive and negative values indicate bonding and antibonding states, respectively. A value for the overlap population close to zero indicates that there is no significant interaction between the electronic populations of the two atoms [29]. As can be seen in Table 3, a large proportion of Zn−Te bonds overlap population values among the three systems, indicating a mixed ionic-covalent character. As to $Zn_{0.875}Se$, the overlap populations as well as bond lengthes of the Zn−Te (I) decreased. It suggests that Zn vacancy induced changes in the bonding of the nearest neighbor Te atoms and there was decreased covalency in the Zn−Te (I) bonds, which is in good agreement with above atomic population analysis. The bond population of Cu−Te (I) bond is higher than any other Zn−-Te bonds in $Zn_{0.875}Cu_{0.125}Te$, indicating that the covalent interaction is strengthened. Moreover, it should be noted that our calculate bond lengths for Zn−Te or Cu−Te essentially agree with Pyykkö's (i.e., 263.9 Å for Zn−Te, 260.6 Å for Cu−Te) [30], who has found an extremely simple (if not simplistic) way to estimate bond lengths in tetrahedrally coordinated crystals.

The bonding picture can be more vividly illustrated by plotting the charge density maps of specific crystallographic planes. Their electron density distribution map is plotted in the way of the electron density difference map, as presented in Fig. 4. The electron density difference was determined as $\Delta\rho=\{\rho_{crystal}-\sum\rho_{ato}\}$, where $\rho_{crystal}$ and $\rho_{ato}$ are the valence electron densities for the studied compound and the corresponding free atoms, respectively [31]. In general, many isolated atoms are connected together through, i.e., chemical

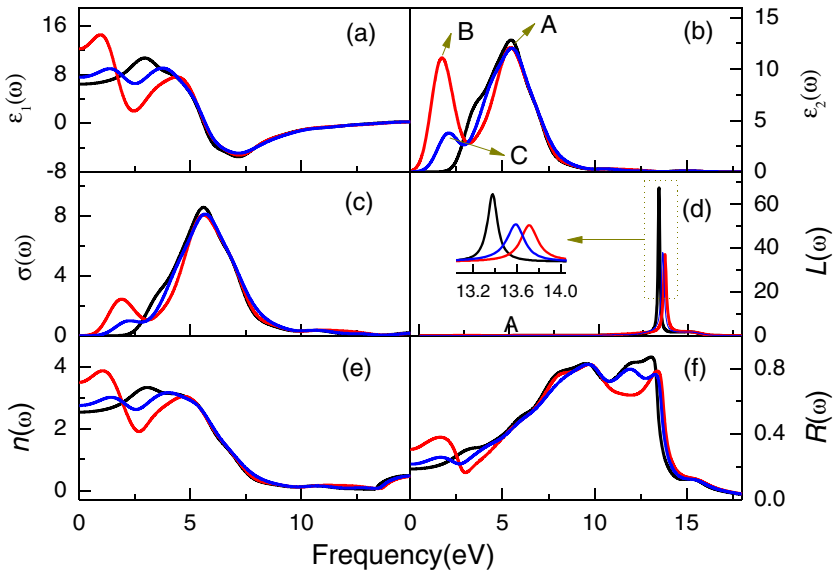


**Fig. 5** Calculated real parts $\varepsilon_1(\omega)$, and imaginary $\varepsilon_2(\omega)$ of dielectric function (**a**∼**b**), conductivity $\sigma(\omega)$ (**c**), energy loss function $L(\omega)$ (**d**), refractive index $n(\omega)$ (**e**), and reflectivity $R(\omega)$ (**f**) for **a** perfect ZnTe (—), **b** $Zn_{0.875}Te$ (—), and **c** $Zn_{0.875}Cu_{0.125}Te$ (—)

**Table 4** Calculated refractive indices $n$ and static dielectric constant $\varepsilon_\infty$

| | $n$ | $\varepsilon_\infty$ |
|---|---|---|
| ZnTe | 2.532 | 6.41 |
| $Zn_{0.875}Te$ | 3.506 | 12.30 |
| $Zn_{0.875}Cu_{0.125}Te$ | 2.746 | 7.54 |

bond to form a solid and liquid. The electron density difference here denotes the difference in the electron density between the bonded atoms and the isolated atoms. This index allows visualizing the electron redistribution of the atoms after chemical bonding. Compare Fig. 4(b) and (c) to Fig. 4(a), it can be seen that the charge density of those Te atoms closest to Zn vacancy is significantly increased, and the charge density of Cu atom is greater than Zn, which is coincided with the Mulliken population analysis.

## Optical properties

Optical property is a key quantity for semiconductors materials with potential applications in photoelectron devices and the semiconductor industry. We already identify that the calculated direct band gap is smaller than the measured value, and the calculated dielectric function shifts toward lower energy. Hence, we amended band gaps by using a scissor operator (scissor: 1.226 eV).

The results of our calculated $\varepsilon_1(\omega)$ are shown in Fig. 5(a). The zero frequency limit of $\varepsilon_1(\omega)$ is the electronic part of the static optical dielectric constant $\varepsilon_1(0)$, which is sometimes denoted as $\varepsilon_\infty$. The calculated $\varepsilon_\infty$ are listed in Table 4. From the table it is clear that $\varepsilon_\infty$ decreases in going from $Zn_{0.875}Te$ to ZnTe. Figure 5(b) depicts the calculated $\varepsilon_2$ ($\omega$) of perfect ZnTe, $Zn_{0.875}Te$, and $Zn_{0.875}Cu_{0.125}Te$ with prominent peaks at the same position A (5.5 eV). These peaks mainly correspond to the transitions from Te 4*p* VBs to the unoccupied CBs as well as Te 4*s* orbitals to the Zn 3*d* or Te 4*p* VBs. As to $Zn_{0.875}Te$, a new peak (B) occurs at 1.74 eV, which may belong to the electron transition from CBs to vacancy acceptor level and cause emission of the red photoluminescence. Similarly, the dielectric peak C (2.05 eV) of $Zn_{0.875}Cu_{0.125}Te$ is attributed to the electron transition from CBs to acceptor impurity level near the top of VBs. The frequency dependent optical conductivity is also calculated and is shown in Fig. 5(c). Optical conduction starts responding to the applied energy field from 2.09 eV, 0.69 eV, and 1.15 eV for ZnTe, $Zn_{0.875}Te$, and $Zn_{0.875}Cu_{0.125}Te$, respectively. Maximum optical conductivity of the investigative materials is at 5.58 eV of magnitude 8.5 $fs^{-1}$. Figure 5(f) shows the results of the reflectivity function $R(\omega)$ for the three materials. The maximum reflectivity occurs in the energy region of [8.0, 13.0 eV], and this is in the ultraviolet region. Thus, the present result suggests that the three structures materials can serve in optical devices such as shields for ultraviolet radiation. Besides, the reflection rates of the three systems reached at 0.8, which is close to 1 and indicates that the systems present metal reflection characteristic with the most incident light reflected. The electron energy loss function $L(\omega)$, which is an important factor describing the energy loss of a fast electron traversing in a material. Prominent peaks in $L(\omega)$ spectra represent the characteristics associated with the plasma oscillations and the corresponding frequencies are the so-called screened plasma frequencies $\omega_p$, which occurs where $\varepsilon_2<1$ and $\varepsilon_1$ reaches zero point [32]. Obviously, one may note from the Fig. 5(d) that the main peaks of $L(\omega)$ are located at about 13.38 eV, 13.58 eV, and 13.72 eV for ZnTe, $Zn_{0.875}Cu_{0.125}Te$, and $Zn_{0.875}Te$, respectively, which correspond to the abrupt reduction of $R(\omega)$ and to the zero crossing of $\varepsilon_1(\omega)$.

The knowledge of the refractive indices of semiconductors is important in the design and analysis of heterostructure lasers and other wave-guiding semiconductor devices. The calculated refractive indices of studied compounds are investigated in Table 4. This is verified by the calculation of the optical dielectric constant $\varepsilon_\infty$, which depends on the $n$. It manifests that within the limits of error the theoretical calculated result for ZnTe were in satisfactory agreement with available experimental value ($n$=2.71) [33], and also meet the rule $\varepsilon_\infty \approx n^2$, mentioned in ref. [34].

## Conclusions

We have applied the GGA within the framework of PP-PW approach to investigate the electronic and optical properties of pure and deficient ZB structures of ZnTe. The choice of compounds was warranted by a great deal of attention given to these semiconductors on account of their large field of applications. The obtained results are well consistent with other theoretical results and the available experimental data.

The calculated results reveal that compared to the perfect ZnTe, the lattice parameters of $Zn_{0.875}Te$ and $Zn_{0.875}Cu_{0.125}Te$ were changed and the cell volumes decreased to some extent due to the vacancy and introduction of impurity. The bonding properties of the two deficient systems are also changed, resulting from the redistribution of electronic charges. A vacancy acceptor level and an acceptor impurity level were produced in $Zn_{0.875}Te$ and $Zn_{0.875}Cu_{0.125}Te$, respectively. Compared with ZnTe, the elongated optical band gap of $Zn_{0.875}Te$ is attributed to the moving toward high energy section of Te 5s state. We observed few differences in band gap between $Zn_{0.875}Cu_{0.125}Te$ and ZnTe, since the Cu *s*-orbital energies are close to that of Zn.

**Acknowledgments** The authors acknowledge the financial support from the Fundamental Research Funds for the Central Universities (CDJZR11220003) and the Science and Technology Planning Project of Liaoning Province (No. 2010220012).

## References

1. Wolf H, Burchard A, Deicher M, Filz T, Jost A, Lauer S, Magerle R, Ostheimer V, Pfeiffer W, Wichert T (1995) Mater Sci Forum 309:196
2. Baron T, Saminadayar K, Magnea N (1998) J Appl Phys 83:1354
3. Soundarajan D, Mangalaraj D, Nataraj D, Dorosinskii L, Kim KH (2012) Mater Lett 87:113
4. Kim JS, Kim HM, Park HL, Choi JC (2006) Solid State Commun 137:115
5. Erlacher A, Ambrico M, Perna G, Schiavulli L (2005) Appl Surf Sci 248:402
6. Joshi KB, Pandya RK, Kothari RK, Sharma BK (2009) Phys Status Solidi B 246:1268
7. Zhou XH, Chen XS, Huang Y, Duan H, Lu W (2006) Phys Status Solidi B 243:1375
8. Szwacki NG, Przeździecka E, Dynowska E, Bogusławski P, Kossut J (2004) Acta Phys Polon A 106:233
9. Uspenskiia Y, Kulatovb E, Mariettec H, Nakayamad H, Ohtae H (2003) J Magn Magn Mater 258:248
10. Tablero C (2010) Comput Mater Sci 49:368
11. Boyer-Richard S, Robert C, Gerard L, Richters JP, Andre R, Bleuse J, Mariette H, Even J, Jancu JM (2012) Nanoscale Res Lett 7:543
12. Ley L, Pollak RA, Mcfeely FR, Kowalczy SP, Shirley DA (1974) Phys Rev B 9:600
13. Payne MC, Teter MP, Allan DC, Arias TA, Joannopoulos JD (1992) Rev Mod Phys 64:1045
14. Vanderbilt D (1990) Phys Rev B 41:7892
15. Perdew JP, Burke K, Ernzerhof M (1996) Phys Rev Lett 77:3865
16. Monkhorst HJ, Pack JD (1976) Phys Rev B 13:5188
17. Fischer TH, Almlof J (1992) J Phys Chem 96:9768
18. Zheng C, Tao Y, Cao JZ, Chen RF, Zhao P, Wu XJ, Huang W (2012) J Mol Model 18:4929
19. Reshak AH, Auluck S (2003) Phys Rev B 68:125101
20. O'Donnell M, Jaynes ET, Miller JG (1981) J Acoust Soc Am 69:696
21. Mo SD, Ching WY (1998) Phys Rev B 57:15219
22. Guo L, Hu G, Feng WJ, Zhang ST (2013) Acta Phys -Chim Sin 29:929
23. Fan SW, Yao KL, Liu ZL (2009) Appl Phys Lett 94:152506
24. Soykan C, Kart SO (2012) J Alloys Compd 529:148
25. Srivastava GP, Weaire D (1987) Adv Phys 36:463
26. Maksimoy O, Tamargo MC (2001) Appl Phys Lett 79:782
27. Rashkeev SN, Lambrecht WRL (2001) Phys Rev B 63:165212
28. Wei SH, Zunger A (1988) Phys Rev B 37:8958
29. Segall MD, Shah R, Pickard CJ, Payne MC (1996) Phys Rev B 54:16317
30. Pyykkö P (2012) Phys Rev B 85:024115
31. Guo L, Hu G, Zhang ST, Feng WJ, Zhang ZP (2013) J Alloy Compd 561:12
32. de Almeida JS, Ahuja R (2006) Phys Rev B 73:165102
33. Marple DTF (1964) J Appl Phys 35:539
34. Samara GA (1983) Phys Rev B 27:3494